Chinese Chemical Letters 33 (2022) 4350–4356

Contents lists available at ScienceDirect

Chinese Chemical Letters

journal homepage: www.elsevier.com/locate/cclet

Surface modification of hollow capsule by Dawson-type polyoxometalate as sulfur hosts for ultralong-life lithium-sulfur batteries

Mingliang Wang, Di Yin, Yundong Cao, Xinyang Dong, Guanggang Gao*, Xun Hu, Cheng Jin, Linlin Fan*, Jian Yu, Hong Liu*

School of Materials Science and Engineering, Collaborative Innovation Center of Metal Nanoclusters & Photo/Electro-Catalysis and Sensing, University of Jinan, Ji'nan 250022, China

ARTICLE INFO

Article history:
Received 16 September 2021
Revised 27 October 2021
Accepted 16 November 2021
Available online 18 November 2021

Keywords:
Polyoxometalates
Hollow capsule shell
Catalytic activity
Chemical bonding
Lithium-sulfur batteries

ABSTRACT

Reasonable construction of sulfur host with high conductivity, large sulfur storage gap, strong chemical adsorption, and fast oxidation–reduction kinetics of polysulfide is very significant for its practical use in lithium-sulfur batteries (LSBs). In this paper, the surface modification of MIL-88A(Fe) is carried out by Dawson-type polyoxometalate (POM), and a hollow capsule shell material with P_2W_{18}, Fe_3O_4, and C components is synthesized by the subsequent carbonization process. When applied as the sulfur host, the hollow capsule shell material can efficiently improve the conductivity of sulfur electrode and restrain the volumetric change of active sulfur while charging and discharging. On this foundation, electrochemical analysis and density functional theory (DFT) calculation show that the P_2W_{18} on the outer layer of the capsule shell have effective electrocatalytic activity and potent chemical bond on the lithium polysulfides (LiPSs), which is helpful to block the shuttle effect. Therefore, the as-assembled LSBs display the outstanding specific capacity and prominent cycle stability. Specifically, it delivers an excellent reversible capacity of 1063 mAh/g after 100 cycles of charge–discharge at a rate of 0.5 C, accounting for a preservation by 96% in comparison to that of the initial cycle. Moreover, even after 2000 cycles at 1 C, the reversible specific capacity of 585 mAh/g can still be maintained with an average decay rate of only 0.021%.

The demands of large-scale energy storage systems and portable electronic devices present the growing trend at present, which motivates the search for energy conversion systems with high energy density and power density [1]. Notably, lithium-sulfur batteries (LSBs) are considered to be one of the most potential next generation high-energy battery systems because of its excellent energy density and theoretical capacity [2,3]. Nevertheless, the LSBs are still prevented by some thorny problems in practical commercial application: (1) the inferior conductivity of sulfur and its lithiation product (Li_2S) causes the slow redox kinetics and low sulfur utilization, and thus limits the rate capacity; (2) the shuttle behavior of discharge intermediates (lithium polysulfides, LiPSs) dissolved in the electrolyte leads to poor cycle durability and low Coulomb efficiency (shuttle effect); (3) the serious volume expansion (about 80%) of sulfur in the lithiation can result in the structure collapse during the charge/discharge cycle [4–6].

To circumvent the above challenges, mammoth effort has been geared to promote the electrochemical properties of LSBs [7,8], including the construction of superior sulfur hosts [9,10], the development of functional membranes or modified interlayer, and the optimization of electrolyte additives [11]. Among the reported strategies, the design of carbon-based matrix materials as the sulfur hosts is feasible, which can raise the electric conductivity and restrain the volume expansion of sulfur electrode to some extent [12–14]. However, these carbon-based sulfur host materials cannot offer strong chemical affinity with polysulfide species, which seriously affect the cycle life of the LSBs [15,16]. Furthermore, according to previous reports, polar inorganic metal-based compounds could supply rich polar active sites for the capture of LiPSs (such as metal nitrides, phosphides, carbides, sulfides, oxides) [17–24]. For example, Zhang *et al.* prepared InN nanowires to modify the separators in LSBs. Both the electron-abundant nitrogen and indium cation of InN act as the polysulfide traps *via* robust chemi-

* Corresponding authors.
E-mail addresses: mse_gaogg@ujn.edu.cn (G. Gao), mse_fanll@ujn.edu.cn (L. Fan), mse_liuh@ujn.edu.cn (H. Liu).

https://doi.org/10.1016/j.cclet.2021.11.043
1001-8417/

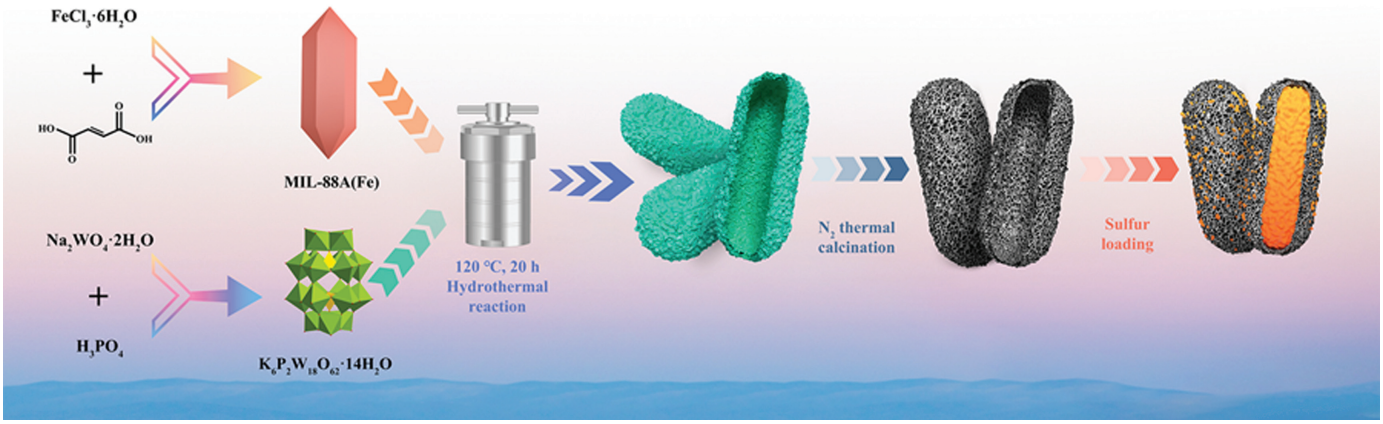

Scheme 1. The synthetic procedure of hollow capsule sulfur host.

cal interaction. At the same time, in the process of electrochemical reaction, the fast electron transfer on polar InN surface expedites the transformation of polysulfides. Hence the InN can efficaciously subdue the shuttle effect [25]. Sun's group demonstrated nitrogen-doped carbon nanosheets/molybdenum phosphide nanocrystal hollow nanospheres, which can be used as an electrochemical catalyst to intensify the redox reaction kinetics of LiPSs and reduce Li_2S nucleation/dissolution interfacial energy barrier [26].

As we all know, polyoxometalates (POMs) have been widely used in the electrochemical field due to their good proton transfer ability and catalytic activity [27–33]. However, there are few reports on the application of POMs in LSBs. Specifically, Yao *et al*. synthetized bifunctional separators constituted of Keggin $[PW_{12}O_{40}]^{3-}$/Super P composite retarding layer, the POMs can act as a Lewis acid site to further enhance the adsorption of the polysulfides [34]. Ye and co-workers found that the LiPSs can be intensively adsorbed on the $\{Ag^{I}PW_{11}O_{39}\}$ cluster by spectroscopic investigations, and the Ag(I) ion of POMs cluster can be used as a Lewis acid site to robustly assimilate S-moieties [35]. More interestingly, Choi *et al*. designed a series of POMs, which were used in sulfur electrode. They found that POMs have multiplicate redox potentials containing the range of equilibrium potentials for sulfur redox processes, which was beneficial to accelerate charge and discharge reactions. Density functional theory (DFT) calculations revealed that the redox potentials of POMs are adjustable, which allowed the optional design of appropriate POMs for specific battery systems [36]. Furthermore, metal–organic frameworks (MOFs) are a class of crystalline organic–inorganic hybrid materials with large specific surface area, high porosity, and excellent stability, which show the application potential in hydrogen storage, catalysis, electrochemistry, and sensors. According to previous reports, MOFs, such as ZIF-8, HKUST-1, and ZIF-67 [37–39] were fabricated and annealed into hierarchical porous carbon as host carriers of sulfur cathode. The resulting carbon materials with porous structure and high specific surface area were beneficial to the sulfur confinement. Therefore, we speculate that it should be possible to exploit MOF–POM hybrids for practical application of LSBs.

Motivated by the above considerations, we have designed a hollow capsule shell containing P_2W_{18} ($K_6P_2W_{18}O_{62}\cdot14H_2O$, a classic Dawson-type POM), Fe_3O_4, and C components derived from MIL-88A(Fe)/P_2W_{18} hybrids by chemical etching and carbonization. MIL-88A(Fe)-derived carbon shell surface has hierarchical porous structure and the partial sulfur confinement in ultra-small mesoporous carbon, combined with hollow capsule structure, guaranteeing the high sulfur loading and effectively suppressing volume expansion of the sulfur upon cycling. More significantly, P_2W_{18} on the surface of capsule shell, as a dual-function assistant, can not only have the strong chemical adsorption for polysulfide, but also show the effective catalytic activity for LiPSs. Benefiting from these favorable factors, in the present study, the hollow capsule shell utilized as a multi-functional sulfur host exhibits superior reversible capacity, extraordinary rate capability and long-life cycle stability. When the current density is set as 0.5 C (1 C = 1675 mAh/g), the specific capacity of 1063 mAh/g can be reached upon 100 cycles. More strikingly, it can be stabilized for 2000 cycles at 1 C, in which the average attenuation rate of per cycle is only 0.021%.

In this work, the synthesis procedure of hollow capsule shell is shown in Scheme 1. MIL-88A(Fe) is initially synthesized by the method reported in the literature [40] and used as the template material. Then P_2W_{18} is successfully loaded on the surface of MIL-88A(Fe) nanorods by hydrothermal reaction. Under acidic conditions, the combination between Fe^{3+} and organic ligands is weakened due to the presence of P_2W_{18}, and thus MIL-88A(Fe) slowly releases Fe^{3+}. The Fe^{3+} can be adsorbed on the surface of MIL-88A(Fe) *via* P_2W_{18}. Due to the Kirkendall effect [41], the diffusion speed of Fe^{3+} in MIL-88A(Fe) is greater than that in solution, therefore, a cavity structure appears in the interior of MIL-88A(Fe), forming the MIL-88A(Fe)/P_2W_{18} composite with the hollow capsule structure. Subsequently, MIL-88A(Fe)/P_2W_{18} is carbonized to obtain composite containing P_2W_{18}, Fe_3O_4, and C, and the original hollow capsule shell structure can be well retained. Finally, the sulfur monomer is diffused into the capsule shell material by melt diffusion method.

The morphology characteristics and crystalline structures of samples are determined. As shown in Fig. 1a, the length and width of MIL-88A(Fe) nanorods with smooth and dense surface are about 2 μm and 500 nm, respectively. After surface modification and etching of MIL-88A(Fe), the hollow capsule shell-shaped MIL-88A(Fe)/P_2W_{18} composite can be obtained (Fig. S1a in Supporting information). In Fig. S2 (Supporting information), it can be observed from Fourier transform infrared spectroscopy (FTIR) that the main peak position of MIL-88A(Fe) do not change significantly after being modified by P_2W_{18}, demonstrating that the structure of MIL-88A(Fe) template is not destroyed after etching. The characteristic peaks of W−O group (910, 943, and 1075 cm^{-1}) can be clearly observed from MIL-88A(Fe)/P_2W_{18}, which confirms that P_2W_{18} is modified on the surface of MIL-88A(Fe) shell. In order to detect the crystal structure and phase purity, X-ray diffraction (XRD) analysis of MIL-88A(Fe), P_2W_{18}, and MIL-88A(Fe)/P_2W_{18} is performed (Fig. S3 in Supporting information). As observed, the diffraction peaks of MIL-88A(Fe) are identical with

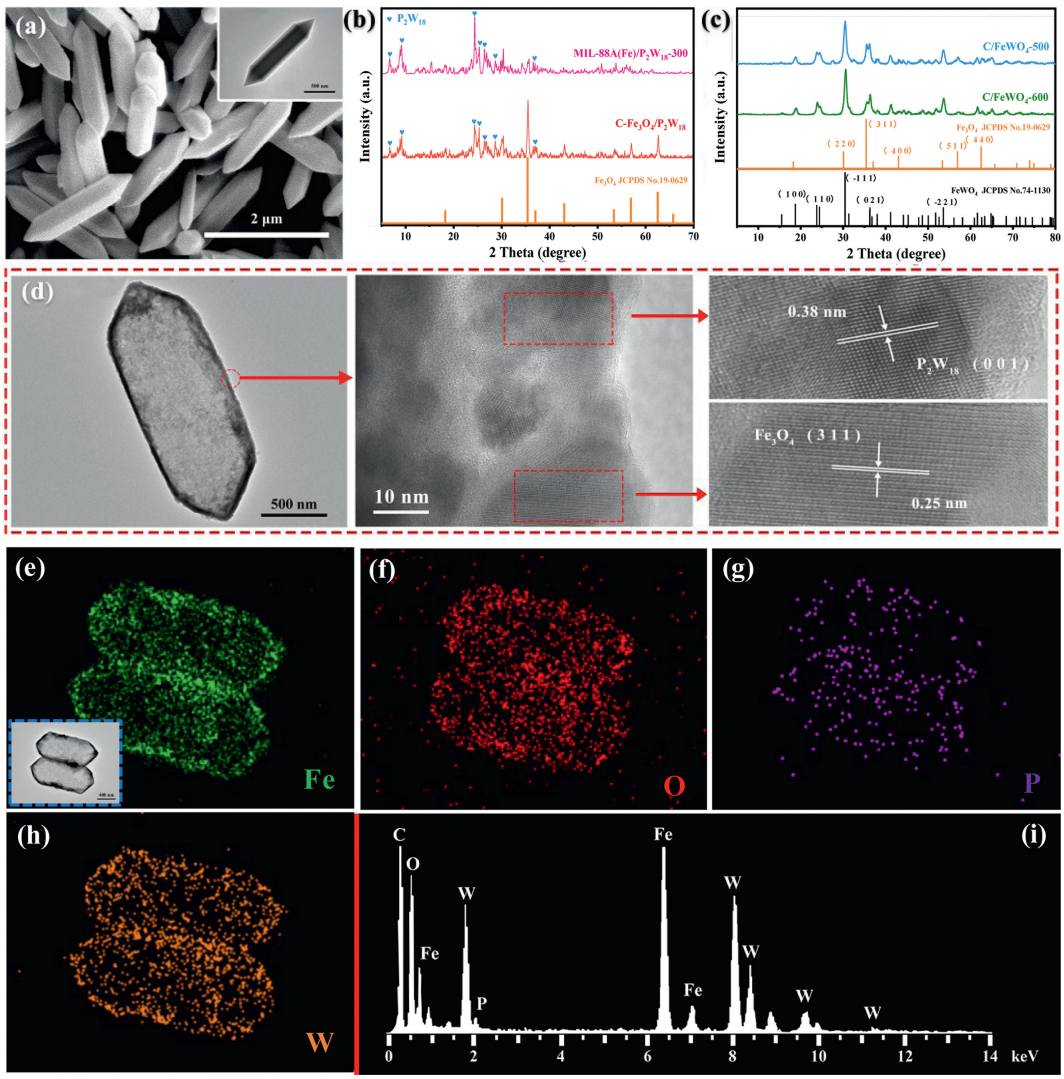

Fig. 1. (a) SEM image of MIL-88A(Fe) (the insert is TEM image). (b) XRD patterns of MIL-88A(Fe)/P_2W_{18}-300 and C-Fe_3O_4/P_2W_{18}. (c) XRD patterns of C/$FeWO_4$-500 and C/$FeWO_4$-600. (d) TEM and HRTEM images of C-Fe_3O_4/P_2W_{18}. The elemental mapping of (e) Fe, (f) O, (g) P, and (h) W of C-Fe_3O_4/P_2W_{18}. (i) EDX spectrum of C-Fe_3O_4/P_2W_{18}.

the data published in references [42], suggesting that a relatively pure MIL-88A(Fe) template. For MIL-88A(Fe)/P_2W_{18}, the characteristic diffraction peaks of P_2W_{18} are clearly displayed, which further illustrates that P_2W_{18} is successfully modified on MIL-88A(Fe). Moreover, the loading amount of P_2W_{18} is calculated to be 30.25 wt% *via* inductively coupled plasma optical emission spectrometer (ICP-OES) (Table S1 in Supporting information). Subsequently, MIL-88A(Fe)/P_2W_{18} composites are carbonized at 300, 400, 500, and 600 °C. Due to the insufficient carbonization at 300 °C, one can see from the XRD patterns (Fig. 1b) that there are no obvious changes compared with MIL-88A(Fe)/P_2W_{18}, and the resulting material can be marked as MIL-88A(Fe)/P_2W_{18}–300. When the calcination temperature is 400 °C, the diffraction peaks of P_2W_{18} and Fe_3O_4 can be clearly observed (marked as C-Fe_3O_4/P_2W_{18}). The peaks at 6.44°, 9.35°, 24.69°, 25.38°, 27.35°, 29.07°, and 35.93° correspond to the index numbers of P_2W_{18} (100), (−111), (223), (204), (115), (−404), and (−307), respectively. Meanwhile, diffraction peaks at 18.27°, 30.09°, 35.42°, 43.05°, 53.39°, 56.94°, and 62.52° correspond to the index numbers of Fe_3O_4 (110), (220), (311), (400), (422), (511) and (440), respectively. Furthermore, as shown in Fig. S4 (Supporting information), the characteristic peaks of MIL-88A(Fe) cannot be found from FTIR of C-Fe_3O_4/P_2W_{18}, suggesting the sufficient carbonization of MIL-88A(Fe) at 400 °C. Fig. S5 exhibits that the content of C in C-Fe_3O_4/P_2W_{18} composite is calculated to be 6.8 wt%. When the temperature continues to rise to 500 °C and 600 °C (Fig. 1c), no diffraction peaks of P_2W_{18} are observed due to the higher carbonization temperature, and the diffraction peaks of $FeWO_4$ are existent, which indicates the disintegration of P_2W_{18}, thus the obtained materials are marked as C/$FeWO_4$-500 and C/$FeWO_4$-600, respectively. Furthermore, MIL-88A(Fe)/P_2W_{18}-300 and C-Fe_3O_4/P_2W_{18} maintain the original hollow capsule shell structure with uniform distribution (Fig. 1d and Fig. S1b in Supporting information). With the temperature increasing, the surface of C/$FeWO_4$-500 is slightly fragmented, and the framework of C/$FeWO_4$-600 is completely fractured and collapsed (Figs. S1c and d in Supporting information). Based on the points discussed above, C-Fe_3O_4/P_2W_{18} presents the optimizational carbonization and retains the original hollow capsule shell structure. When employed as the sulfur host, C-Fe_3O_4/P_2W_{18} hollow capsule can relieve the volume change of sulfur cathode and achieve high sulfur loading. The high resolution transmission electron microscopy (HRTEM) images in Fig. 1d demonstrate that the lattice fringe spacings of 0.38 nm and 0.25 nm agree well with (001) plane of P_2W_{18} and (311) plane of Fe_3O_4, which proves the high crystallinity of P_2W_{18} and Fe_3O_4. Moreover, the elemental mapping and energy-dispersive X-ray spectroscopy (EDX) of C-Fe_3O_4/P_2W_{18}

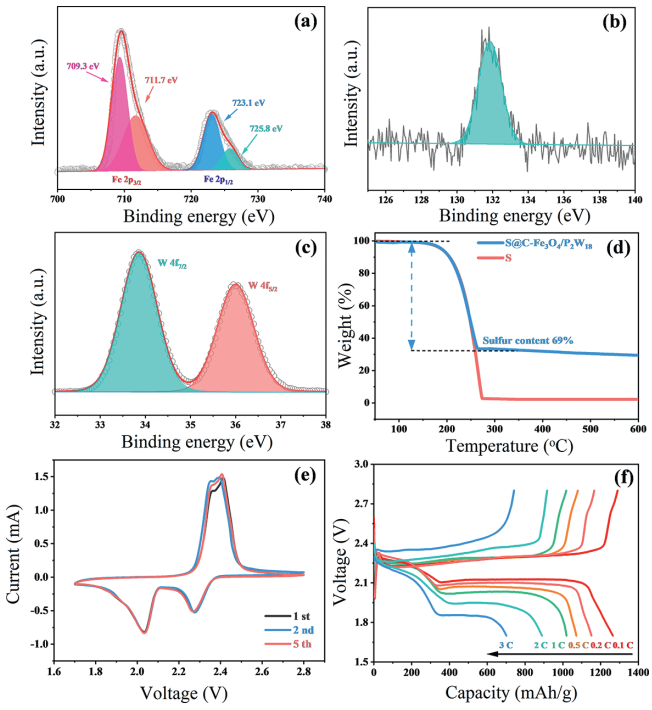

Fig. 2. XPS analysis of C-Fe_3O_4/P_2W_{18}: (a) Fe 2p spectra, (b) P 2p spectra, and (c) W 4f spectra. (d) TGA curves of bare S and S@C-Fe_3O_4/P_2W_{18}. (e) CV curves of S@C-Fe_3O_4/P_2W_{18} electrode at a scan speed of 0.1 mV/s. (f) Galvanostatic charge–discharge curves of S@C-Fe_3O_4/P_2W_{18} electrode at current densities from 0.1 C to 3 C.

show that Fe, O, P, and W elements are uniformly distributed in the shell layer (Figs. 1e–i).

The surface chemistry environment of C-Fe_3O_4/P_2W_{18} is further analysed by X-ray photoelectron spectroscopy (XPS). Fig. S6 (Supporting information) presents typical survey spectra, strong W, P, C, Fe, and O signals can be observed. The high resolution XPS spectra of Fe 2p are revealed in Fig. 2a, the peaks at 709.3 eV/711.7 eV and 723.1 eV/725.8 eV belong to the Fe $2p_{3/2}$ and Fe $2p_{1/2}$ orbital double peaks, respectively, confirming the formation of Fe_3O_4. The peak position at 131.9 eV in Fig. 2b is in accord with binding energy of P 2p, and the characteristic peaks at 33.9 eV and 36.0 eV are corresponding to W $4f_{7/2}$ and W $4f_{5/2}$ (Fig. 2c), respectively, suggesting P_2W_{18} can exist stably after the etching and carbonization process. Subsequently, C-Fe_3O_4/P_2W_{18} is used as a sulfur host material, the sulfur can diffuse into C-Fe_3O_4/P_2W_{18} by melt diffusion method (marked as S@C-Fe_3O_4/P_2W_{18}), and the XRD pattern shows the obvious diffraction peaks of sulfur (Fig. S7 in Supporting information). As shown in Figs. S8 and S9 (Supporting information), the S@C-Fe_3O_4/P_2W_{18} retains the original capsule shell structure. The sulfur particles accumulate inside the hollow thin shell with the large voids, and partial sulfur can be absorbed on the capsule shell surface. Moreover, the Brunauer-Emmett-Teller (BET) surface areas of C-Fe_3O_4/P_2W_{18} and S@C-Fe_3O_4/P_2W_{18} are obtained by nitrogen isothermal adsorption-desorption curve analysis (Fig. S10 in Supporting information). Compared with C-Fe_3O_4/P_2W_{18} (214 m^2/g), S@C-Fe_3O_4/P_2W_{18} presents a relatively small specific surface area (2.26 m^2/g), suggesting the high surface utilization rate of C-Fe_3O_4/P_2W_{18} as well as the uniform loading of sulfur.

Apparently, the hollow capsule shell of C-Fe_3O_4/P_2W_{18} not only can be used as the host with high sulfur content, but also can be beneficial to accelerate rapid transport of lithium ions due to its porous conductive network. Furthermore, P_2W_{18} on the surface of the capsule shell exhibits strong adsorption ability and favorable electrochemical catalysis for LiPSs (will be further discussed). Elemental mapping results (Fig. S11 in Supporting information) further display that Fe, W, O, P, C, and S elements are evenly distributed in S@C-Fe_3O_4/P_2W_{18}. Thermogravimetric analysis (TGA) is carried out to ascertain the active sulfur content in S@C-Fe_3O_4/P_2W_{18}. One can see from Fig. 2d that the sulfur loading in S@C-Fe_3O_4/P_2W_{18} is 69 wt%. Fig. 2e reveals cyclic voltammetry (CV) curves of S@C-Fe_3O_4/P_2W_{18} cathode in the potential range of 1.7–2.8 V at 0.1 mV/s. Clearly, two couple of redox characteristic peaks emerge in the cathode scan and anode scan, suggesting that there are multiple reaction mechanisms in LSBs. The cathodic characteristic peaks at 2.31 V and 2.03 V correspond to the formation of higher order Li_2S_x ($4 \leq x \leq 8$) and further electrochemical reduction to insoluble Li_2S_2/Li_2S, respectively. The anodic scans reveal two peaks near 2.37 V and 2.42 V, representing the oxidation of Li_2S_2/Li_2S to long-chain Li_2S_x and the final oxidation to elemental sulfur, respectively. Galvanostatic discharge/charge experiments of S@C-Fe_3O_4/P_2W_{18} electrode at the current densities of 0.1–3 C are studied (Fig. 2f). Clearly, the discharge/charge profiles at each current rate display two pairs of redox peaks, which matches the test results of CV. Moreover, it delivers reversible capacities of 1289.7, 1151.5, 1071.3, 1019.4, 889.4, and 701.7 mAh/g at 0.1, 0.2, 0.5, 1, 2, and 3 C, respectively, showing excellent electrochemical performance.

S@MIL-88A(Fe)/P_2W_{18}–300, S@C/$FeWO_4$–500, and S@C/$FeWO_4$–600 electrodes are prepared by the same method for S@C-Fe_3O_4/P_2W_{18}. Fig. 3a exhibits the initial galvanostatic discharge/charge profiles of as-prepared products at 0.1 C. S@C-Fe_3O_4/P_2W_{18} presents the lowest polarization value (ΔV) of 176 mV than that of S@MIL-88A(Fe)/P_2W_{18}–300 (263 mV), S@C/$FeWO_4$–500 (244 mV), and S@C/$FeWO_4$–600 (252 mV). The low polarization demonstrates the fast electrochemical reaction kinetics and increased catalytic activity, accelerating the facile conversion of LiPSs and guaranteeing the sufficient utilization of active sulfur [43]. Fig. 3b compares the cycling performance of S@MIL-88A(Fe)/P_2W_{18}-300, S@C-Fe_3O_4/P_2W_{18}, S@C/$FeWO_4$-500, and S@C/$FeWO_4$-600 electrodes at current density of 2 C in a voltage range of 1.7–2.8 V. Note that S@MIL-88A(Fe)/P_2W_{18}–300 exhibits poor cycle life and it falls to 414 mAh/g after 100 cycles. The poor performance of S@MIL-88A(Fe)/P_2W_{18}-300 results from the insufficient carbonization, which cannot guarantee outstanding conductivity of sulfur cathode. Whereas, with the increasing of carbonization temperature, the reversible capacities of S@C/$FeWO_4$-500 and S@C/$FeWO_4$-600 are obviously enhanced, which remain stable at around 534 and 558 mAh/g when the test is prolonged to 100 cycles. However, as mentioned above, the higher carbonization temperature results in the collapse of hollow capsule shell structure, causing the low sulfur utilization. Meanwhile, the large volume change of sulfur cathode during lithiation–delithiation cycles cannot be restrained. Fortunately, the reversible capacity of S@C-Fe_3O_4/P_2W_{18} continuously decreases from the 1st cycle to the 25th cycle, while its discharge capacity tends to be stable from the 26th cycle to the 160th cycle. The discharge capacity in the 160th cycle (710 mAh/g) accounts for a retention by 91% in comparison to that of the 25th cycle (783 mAh/g). Therefore, S@C-Fe_3O_4/P_2W_{18} with optimizational carbonization presents the best cycling performance for all as-prepared products because of its integrity of hollow capsule shell structure, excellent conductivity, and the higher sulfur loading. For comparison, the C-Fe_3O_4 composites are synthesized by carbonizing MIL-88A(Fe) at 400 °C for 2 h The morphological and structural features are displayed in Figs. S12 and S13 (Supporting information), and it can be noticed that C-Fe_3O_4 presents the rod-like structure with diameter of 500 nm and length of 2 μm. BET surface area and pore size distribution curves on C-Fe_3O_4/P_2W_{18} and C-Fe_3O_4 are shown in Fig. S14 (Supporting information). One can see that the specific surface area

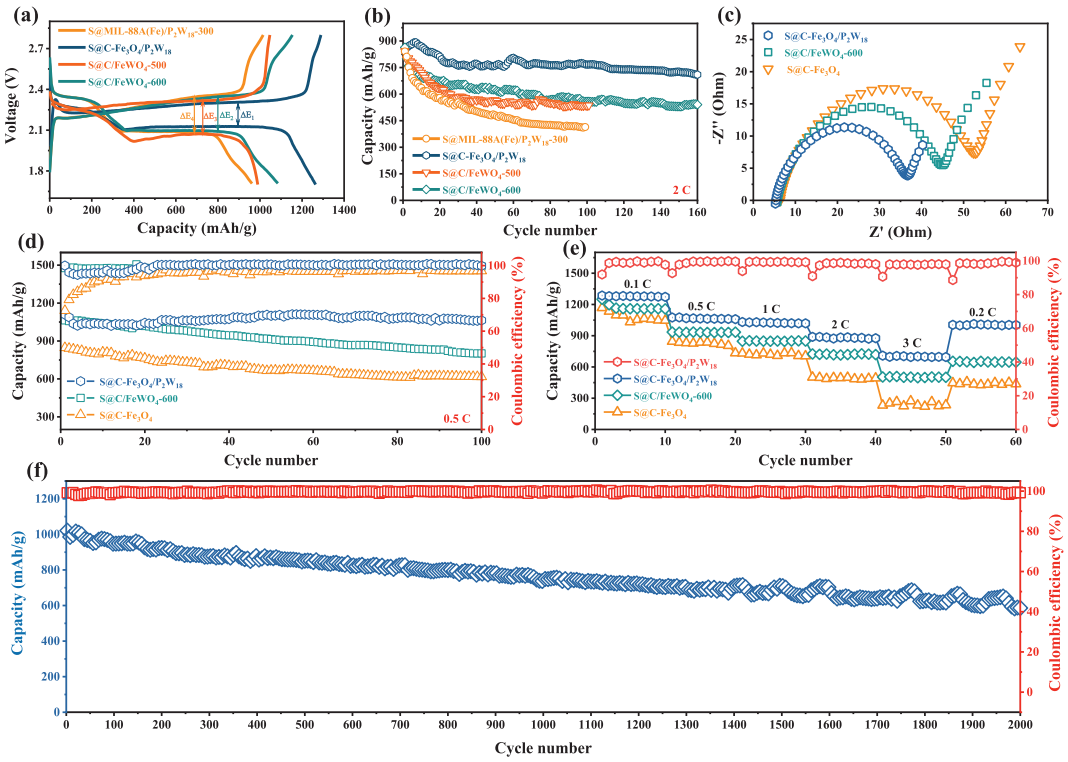

Fig. 3. (a) The initial charge–discharge curves of S@MIL-88A(Fe)/P_2W_{18}-300, S@C-Fe_3O_4/P_2W_{18}, S@C/$FeWO_4$-500, and S@C/$FeWO_4$-600 electrodes at 0.1 C. (b) Cycle performance of S@MIL-88A(Fe)/P_2W_{18}-300, S@C-Fe_3O_4/P_2W_{18}, S@C/$FeWO_4$-500, and S@C/$FeWO_4$-600 electrodes at 2 C. (c) Nyquist plots of S@C-Fe_3O_4/P_2W_{18}, S@C/$FeWO_4$-600, and S@C-Fe_3O_4 electrodes. (d) Cycle performance of S@C-Fe_3O_4/P_2W_{18}, S@C/$FeWO_4$-600, and S@C-Fe_3O_4 electrodes at 0.5 C. (e) Rate performance of S@C-Fe_3O_4/P_2W_{18}, S@C/$FeWO_4$-600, and S@C-Fe_3O_4 electrodes at current densities from 0.1 C to 3 C. (f) Long-life cycling performance of the S@C-Fe_3O_4/P_2W_{18} at 1 C.

of C-Fe_3O_4/P_2W_{18} is greater than that of C-Fe_3O_4 (130 m^2/g). Besides, the pore size of approximately 20 nm is determined for C-Fe_3O_4/P_2W_{18}. The mesoporous structure with large specific surface area not only furnishes a more active pathway for sulfur adsorption and conversion, but also effectively relieves sulfur cathode expansion/shrinkage upon cycling. Based on above results, electrochemical impedance spectroscopy (EIS) tests are determined to research the interfacial charge transfer processes in the fresh cells. The Nyquist plots present a semicircle in the high-frequency region and one sloped line at low-frequency location, as depicted in Fig. 3c. One can see that S@C-Fe_3O_4/P_2W_{18} (37 Ω) shows the low charge transfer resistance compared with S@C-Fe_3O_4 (54 Ω) and S@C/$FeWO_4$-600 (46 Ω), confirming the high conductivity of S@C-Fe_3O_4/P_2W_{18} and the rapid electron transport by P_2W_{18} catalyst (will be further discussed) [44,45].

Moreover, the cycle performance of S@C-Fe_3O_4/P_2W_{18}, S@C/$FeWO_4$-600, and S@C-Fe_3O_4 is conducted at 0.5 C *via* galvanostatic measurements (Fig. 3d). Capacity of S@C/$FeWO_4$-600 fades from 1067 mAh/g to 801 mAh/g upon 100 cycles. In addition, the S@C-Fe_3O_4 also displays poor cycle life. As expected, S@C-Fe_3O_4/P_2W_{18} achieves a superior discharge specific capacity of 1108 mAh/g in the 1st cycle. More strikingly, for S@C-Fe_3O_4/P_2W_{18} electrode, the retentive capacity of 1063 mAh/g up to 100 cycles is 96% of the initial cycle capacity, showing outstanding electrochemical stability. While capacity retention values of S@C/$FeWO_4$-600 and S@C-Fe_3O_4 are 75% and 72%, respectively. Besides, the average Coulombic efficiency of S@C-Fe_3O_4/P_2W_{18} electrode is more than 99% in the process of cycling, which is higher than that of S@C/$FeWO_4$-600 (96%). More obviously, the Coulombic efficiency of S@C-Fe_3O_4 fluctuates greatly, and the average Coulombic efficiency is only 93%. To further illustrate the structure of S@C-Fe_3O_4/P_2W_{18} upon cycling, the electrochemical cells after 100 discharge–charge cycles at 0.5 C are disassembled in the argon-filled glovebox, and their morphologies are observed by transmission electron microscopy (TEM) and scanning electron microscopy (SEM) (Figs. S15 and S16 in Supporting information). As expected, the robust capsule shell structure is basically preserved, guaranteeing the excellent electrochemical performance. Moreover, EIS tests are carried out after cycling at 0.5 C for 100 cycles (Fig. S17 in Supporting information). The charge transfer resistance of S@C-Fe_3O_4/P_2W_{18} is still significantly lower than that of S@C-Fe_3O_4 and S@C/$FeWO_4$-600, which suggests the smallest electrochemical reaction polarization and excellent conductivity during repeated lithiation-delithiation cycles. S@C-Fe_3O_4/P_2W_{18} also displays the better rate performance under different current densities than that of S@C/$FeWO_4$-600 and S@C-Fe_3O_4 (Fig. 3e). When the current densities increase from 0.1 C to 0.5, 1, 2, and 3 C, the specific capacities of S@C-Fe_3O_4/P_2W_{18} cathode decrease slightly from 1286 to 1075, 1032, 889, and 709 mAh/g. The lower capacity fading rate is comparable to the recent reports for other multi-function sulfur hosts (Fig. S18 in Supporting information). Specifically, when the current density is recovered to 0.2 C, the discharge specific capacity could be restored to 1014 mAh/g, which indicates the high electrochemical reversibility. However, the cells based on S@C/$FeWO_4$-600 and S@C-Fe_3O_4 cathodes show significantly fast capacity decay rates and maintain the specific capacities of only 511 and 296 mAh/g at 3 C, respectively. Based on superior cyclic capability and rate performance of S@C-Fe_3O_4/P_2W_{18}, long-term cycle stability is indispensable for practical applications of LSBs. In Fig. 3f, the discharge specific capacity decreases slowly when S@C-Fe_3O_4/P_2W_{18} electrodes are cycled at 1 C, retaining a capacity of 585 mAh/g even after 2000 deep cycles. The ultralow capacity decay of 0.021% per cycle is obtained, which is better than many other sulfur cathodes with metal-based hosts (Table S2 in Supporting information). Meanwhile, the Coulombic efficiency of S@C-Fe_3O_4/P_2W_{18} electrode is more than 98% in the process of

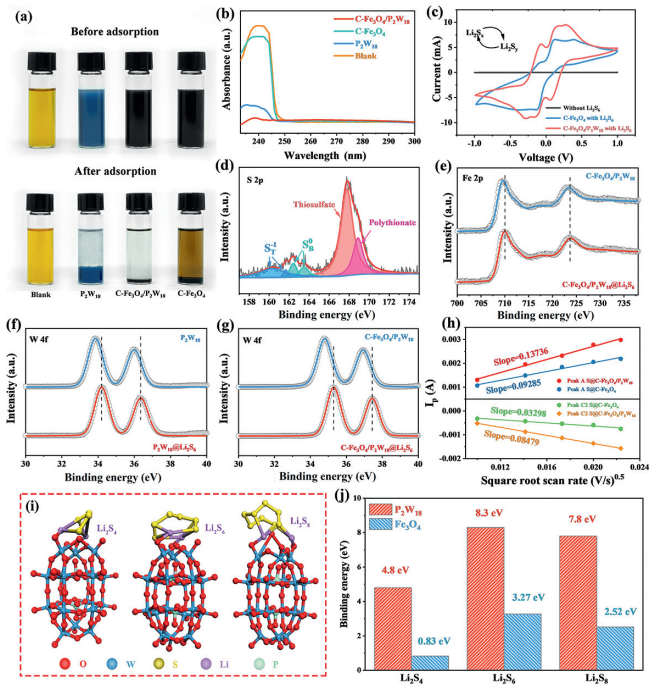

Fig. 4. (a) Optical observation and (b) UV–vis spectra of Li_2S_6 solution adsorbed by C-Fe_3O_4/P_2W_{18}, C-Fe_3O_4, and P_2W_{18}. (c) CV curves of Li_2S_6 symmetrical cells with C-Fe_3O_4/P_2W_{18} and C-Fe_3O_4 working electrodes. High-resolution XPS analysis of (d) S 2p spectra for P_2W_{18}@Li_2S_6, (e) Fe 2p spectra for C-Fe_3O_4/P_2W_{18} and C-Fe_3O_4/P_2W_{18}@Li_2S_6, (f) W 4f spectra for P_2W_{18} and P_2W_{18}@Li_2S_6, and (g) W 4f spectra for C-Fe_3O_4/P_2W_{18} and C-Fe_3O_4/P_2W_{18}@Li_2S_6. (h) Plots of the peak current versus the square root of scan rate for S@C-Fe_3O_4/P_2W_{18} and S@C-Fe_3O_4. (i) Optimized geometries of Li_2S_4, Li_2S_6, and Li_2S_8 adsorbed on terminal oxygen of P_2W_{18}. (j) Binding energy values for Li_2S_4, Li_2S_6, Li_2S_8 on P_2W_{18} (terminal oxygen) and Fe_3O_4 (311) surface, respectively.

cycling. These results indicate that S@C-Fe_3O_4/P_2W_{18} has excellent ultra-long cycle performance as cathode materials of LSBs.

Li_2S_6 with high solubility in the electrolyte is employed as the representative LiPSs intermediate to examine the polysulfide absorption by the C-Fe_3O_4/P_2W_{18}, P_2W_{18}, and C-Fe_3O_4. As shown in Fig. 4a, the Li_2S_6 and three as-prepared powders are sealed in vials, and then mix the compounds for 6 h, respectively. Clearly, for C-Fe_3O_4/P_2W_{18} and P_2W_{18}, the solution fades to be almost colorless, while no obvious color change is observed for C-Fe_3O_4, proving the strong adsorption ability of P_2W_{18}. The interaction between Li_2S_6 and three as-prepared samples is further verified by the ultraviolet–visible (UV–vis) spectra (Fig. 4b). According to the analysis of supernatant, a strong peak near 240 nm before adsorption is found. The peak intensity decreases slightly after Li_2S_6 solution is adsorbed by C-Fe_3O_4, while the peak intensity decreases significantly after Li_2S_6 solution is adsorbed by C-Fe_3O_4/P_2W_{18} and P_2W_{18}, testifying that P_2W_{18} has stronger adsorption ability for LiPSs. The catalytic effect of C-Fe_3O_4/P_2W_{18} on accelerating the kinetics of polysulfide conversion is investigated using CV tests. As observed in Fig. 4c, the Li_2S_6 symmetric cell based on the C-Fe_3O_4/P_2W_{18} electrode presents six distinct peaks, while the C-Fe_3O_4 electrode shows inconspicuous redox peak pairs and the lower polarization current. These results suggest that the P_2W_{18} sites in C-Fe_3O_4/P_2W_{18} could effectively facilitate the reversible conversion of LiPSs, ensuring the superior redox kinetics and high electrochemical reversibility of C-Fe_3O_4/P_2W_{18}.

To sufficient assess the chemical interaction between P_2W_{18} and polysulfides, XPS analyses are performed on the pristine C-Fe_3O_4/P_2W_{18}, P_2W_{18} and C-Fe_3O_4/P_2W_{18}@Li_2S_6, P_2W_{18}@Li_2S_6 composites after the adsorption experiment (Fig. 4a). Fig. 4d shows the XPS spectra of S 2p in P_2W_{18}@Li_2S_6, the peaks centered at 160.5 eV and 161.8 eV are in accord with terminal sulfur (S_T^{-1}), the peaks at 162.6 eV and 163.7 eV correspond to the bridging sulfur (S_B^0), and signals detected at 167.9 eV and 169.1 eV peaks can be matched to thiosulfate (formed by the oxidation of sulfur in polysulfides) and polypolysulfate complex (formed primarily by the reaction between the anchored polysulfide and thiosulfate, as shown in Eq. 1), respectively [46–48].

$$\left[\begin{array}{c} O \\ \| \\ O-S-S \\ \| \\ O \end{array}\right]^{2-} + Li_2S_x \rightleftarrows \left[\begin{array}{c} O \\ \| \\ O-S-(S)_{x-y}-S-O \\ \| \\ O \end{array}\right]^{2-} + Li_2S_x \quad (x \geq 4, y < 3) \tag{1}$$

The soluble LiPSs (Li_2S_x, $x \geq 4$) can be converted into low solubility polysulfate medium and short-chain polysulfide (Li_2S_y, $y < 3$), which is indicative of the catalytic role of P_2W_{18} to actively promote a series of redox reactions of LiPSs. Fig. 4e is the characteristic spectra of Fe 2p in C-Fe_3O_4/P_2W_{18} and C-Fe_3O_4/P_2W_{18}@Li_2S_6. It can be observed that there is no obvious shift in the peak position. Notably, as an active component in the composites, when P_2W_{18} interacts with Li_2S_6, the binding energy of the two W 4f peaks can be significantly increased. For P_2W_{18} (Fig. 4f), the W 4f peaks shift from the original 33.8 eV/35.9 eV to 34.2 eV/36.3 eV after adsorption of Li_2S_6, while the W 4f peaks in C-Fe_3O_4/P_2W_{18} shift from the original 34.8 eV/36.9 eV to 35.2 eV/37.4 eV after adsorption of Li_2S_6 (Fig. 4g). These phenomena suggest that the active P_2W_{18} can provide suitable polar sites on the capsule shell, facilitating the rapid transfer of electrons through the P_2W_{18} to the exposed sites and finally to the S–S bonds of polysulfides, which is consistent with EIS results shown in Fig. 3c. More importany, the chemical binding formed by the P_2W_{18} can be used as a Lewis acid site to greatly improve the sulfur cathode retention ability and chemically restrict the dissolution and migration behavior of LiPSs, thus restraining the shuttle effect and prolonging the cycle life of the LSBs.

A series of CV curves with scan speeds of 0.1, 0.2, 0.3, 0.4, and 0.5 mV/s are recorded to research the Li^+ diffusion coefficient of S@C-Fe_3O_4/P_2W_{18} and S@C-Fe_3O_4 (Figs. S19a and b in Supporting information). The Li^+ diffusion kinetics can be acquired according to the Randles-Sevcik equation (Eq. 2) [49]:

$$I_P = \left(2.69 \times 10^5\right) n^{1.5} S D_{Li}^{0.5} C_0 \nu^{0.5} \tag{2}$$

where n represents electron number, I_P is the peak current, D_{Li} is the diffusion coefficient of Li^+, S represents electrode area, ν is the scan rate, C_0 is the Li^+ concentration in solution, and the slopes of $I_p/\nu^{0.5}$ curves have positive correlation with D_{Li} [50]. The slope values ($I_p/\nu^{0.5}$) of Peak A, Peak C1, and Peak C2 are calculated in Fig. 4h and Fig. S19c (Supporting information). Note that S@C-Fe_3O_4/P_2W_{18} cathode shows high Li^+ diffusion coefficients compared with S@C-Fe_3O_4, which corresponds to the fast conversion of long-chain LiPSs to Li_2S_2/Li_2S catalyzed by P_2W_{18}, promoting the diffusion of lithium ions to sulfur species. The DFT calculations are conducted to further prove the interaction between P_2W_{18} and LiPSs. Fig. 4i and Fig. S20 (Supporting information) show the adsorption situations of Li_2S_4, Li_2S_6, and Li_2S_8 on P_2W_{18} (terminal oxygen) and Fe_3O_4 (311) surface, respectively. The binding energy (E_{ads}) of LiPSs adsorbing on the P_2W_{18} and Fe_3O_4 molecules is calculated referring to the following Eq. 3:

$$E_{ads} = E_{LiPSs} + E_{P_2W_{18}/Fe_3O_4} - E_{total} \tag{3}$$

where E_{LiPSs} is the surface energy of LiPSs, $E_{P_2W_{18}/Fe_3O_4}$ is the surface energy of P_2W_{18} or Fe_3O_4, and the E_{total} is the total energy of P_2W_{18} or Fe_3O_4 combined with LiPSs. Based on Eq. 3, the positive value of E_{ads} indicates that the corresponding adsorption structure

is energetically beneficial to form [51]. As described in Fig. 4j, the binding energies of Li_2S_4, Li_2S_6, and Li_2S_8 on the P_2W_{18} are calculated to be 4.8, 8.3, and 7.8 eV, and the adsorption energies between polysulfides and Fe_3O_4 are 0.83 eV for Li_2S_4, 3.27 eV for Li_2S_6, and 2.52 eV for Li_2S_8. The higher binding energy means the strong capture ability of P_2W_{18} on LiPSs, which is advantageous to the enhancement of electrochemical performance of LSBs.

In conclusion, the hollow capsule shell with P_2W_{18}, Fe_3O_4, and C components has been successfully synthesized by optimizing the carbonization temperature. When used as the sulfur host, the capsule shell can alleviate the volume change of sulfur cathode among lithiation–delithiation cycles and guarantee the higher sulfur loading. The strong carbon shell is favorable to increase electrical conductivity of sulfur cathode material, and abundant porous structure can accelerate the diffusion and transfer kinetics of lithium ions. What is more, the P_2W_{18} on the capsule shell has impregnable chemical bond and efficient catalytic activity for the LiPSs, which is conducive to facilitate the redox reaction of LiPSs and prevent the shuttle effect. Therefore, S@C-Fe_3O_4/P_2W_{18} cathode achieves high reversible capacity, outstanding rate performance, and ultralong stable life span. This study may stimulate the search for more advanced cathode structures, such as hollow structure doped with POMs, yolk shell or multi-shell particles through the molecular design, to increase the electrochemical property of LSBs with long-life cycle stability.

Declaration of competing interest

The authors declare no conflicts of interests.

Acknowledgments

We gratefully acknowledge the financial support from the National Natural Science Foundation of China (No. 21971085) and the Natural Science Foundation of Shandong Province (No. ZR2019MB004, China).

Supplementary materials

Supplementary material associated with this article can be found, in the online version, at doi:10.1016/j.cclet.2021.11.043.

References

[1] R. Hu, Y. Fang, X. Liu, et al., Chem. Res. Chin. Univ. 37 (2021) 311–317.
[2] A. Manthiram, Y. Fu, S.H. Chung, et al., Chem. Rev. 114 (2014) 11751–11787.
[3] X.R. Han, X.T. Guo, M. Xu, et al., Rare Metals 39 (2020) 1099–1106.
[4] Z.W. Seh, Y. Sun, Q. Zhang, Y. Cui, Chem. Soc. Rev. 45 (2016) 5605–5634.
[5] Z. Sun, J. Zhang, L. Yin, et al., Nat. Commun. 8 (2017) 14627.
[6] S. Jiang, S. Huang, M. Yao, et al., Chin. Chem. Lett. 31 (2020) 2347–2352.
[7] H. Peng, J.Q. Huang, X.B. Cheng, Q. Zhang, Adv. Energy Mater. 7 (2017) 1700260.
[8] R. Fang, S. Zhao, Z. Sun, et al., Adv. Mater. 29 (2017) 1606823.
[9] P. Bonnick, J. Muldoon, Energy Environ. Sci. 13 (2020) 4808–4833.
[10] X. Chen, T. Hou, K.A. Persson, Q. Zhang, Mater. Today 22 (2019) 142–158.
[11] S. Zhang, K. Ueno, K. Dokko, M. Watanabe, Adv. Energy Mater. 5 (2015) 1500117.
[12] J.J. Cai, C. Wu, Y. Zhu, et al., J. Power Sources 341 (2017) 165–174.
[13] T. Liu, L. Zhang, B. Cheng, J. Yu, Adv. Energy Mater. 9 (2019) 1803900.
[14] A. Fu, C. Wang, F. Pei, et al., Small 15 (2019) 1804786.
[15] Y. Song, W. Cai, L. Kong, et al., Adv. Energy Mater. 10 (2019) 1901075.
[16] B. Gao, X. Li, K. Ding, et al., J. Mater. Chem. 7 (2019) 14–37.
[17] R.H. Zhang, C. Chi, M.C. Wu, et al., J. Power Sources 451 (2020) 227751.
[18] Y. Zheng, S. Zheng, H. Xue, H. Pang, J. Mater. Chem. 7 (2019) 3469–3491.
[19] R.H. Zhang, M.C. Wu, X.Z. Fan, et al., J. Power Sources 436 (2019) 226840.
[20] J. He, A. Manthiram, Energy Storage Mater. 20 (2019) 55–70.
[21] B. Yu, Y.F. Chen, Z.G. Wang, et al., J. Power Sources 447 (2020) 227364.
[22] L. Zhang, Y. Wang, Z. Niu, J. Chen, Carbon 141 (2019) 400–416.
[23] Y. Yang, B. Zhang, Y. Wang, et al., J. Am. Chem. Soc. 135 (2013) 14500–14503.
[24] E. Alhajji, W. Wang, W. Zhang, et al., ACS Appl. Mater. Interfaces 12 (2020) 18833–18839.
[25] L. Zhang, X. Chen, F. Wan, et al., ACS Nano 12 (2018) 9578–9586.
[26] Z. Sun, X.L. Wu, Z. Peng, et al., Small 15 (2019) 1902491.
[27] S.T. Zheng, G.Y. Yang, Chem. Soc. Rev. 41 (2012) 7623–7646.
[28] N.V. Izarova, M.T. Pope, U. Kortz, Angew. Chem. Int. Ed. 51 (2012) 9492–9510.
[29] L. Cronin, A. Muller, Chem. Soc. Rev. 41 (2012) 7333–7334.
[30] Y.F. Song, R. Tsunashima, Chem. Soc. Rev. 41 (2012) 7384–7402.
[31] M. Yu, S. Zhou, Z. Wang, et al., Adv. Funct. Mater. 29 (2019) 1905986.
[32] S.S. Wang, G.Y. Yang, Chem. Rev. 115 (2015) 4893–4962.
[33] S.U. Khan, B.L. Liu, M. Akhtar, et al., Inorg. Chem. Commun. 97 (2018) 187–190.
[34] W. Yao, L. Liu, X. Wu, et al., ACS Appl. Mater. Interfaces 10 (2018) 35911–35918.
[35] J.C. Ye, J.J. Chen, R.M. Yuan, et al., J. Am. Chem. Soc. 140 (2018) 3134–3138.
[36] W. Choi, D. Im, M.S. Park, et al., Electrochemistry 84 (2016) 882–886.
[37] Y. Liu, G. Li, J. Fu, et al., Angew. Chem. Int. Ed. 56 (2017) 6176–6180.
[38] H.B. Wu, S. Wei, L. Zhang, et al., Chemistry 19 (2013) 10804–10808.
[39] M. Li, W. Feng, W. Su, et al., J. Solid State Electrochem. 23 (2019) 2317–2324.
[40] X. Liao, F. Wang, F. Wang, et al., Appl. Catal. B: Environ. 259 (2019) 118064.
[41] W. Wang, M. Dahl, Y. Yin, Chem. Mater. 25 (2012) 1179–1189.
[42] H. Wu, M.D. Ma, W.Z. Gai, et al., Environ. Sci. Pollut. Res. Int. 25 (2018) 27196–27202.
[43] L. Ji, X. Wang, Y. Jia, et al., Adv. Funct. Mater. 30 (2020) 1910533.
[44] Y. Wang, R. Zhang, Y. Pang, et al., Energy Storage Mater. 16 (2019) 228–235.
[45] R. Li, H. Peng, Q. Wu, et al., Angew. Chem. Int. Ed. 59 (2020) 12129–12138.
[46] H.Y. Zhou, Z.Y. Sui, K. Amin, et al., ACS Appl. Mater. Interfaces 12 (2020) 13904–13913.
[47] H. Tang, W. Li, L. Pan, et al., Adv. Sci. 5 (2018) 1800502.
[48] S. Chen, J. Luo, N. Li, et al., Energy Storage Mater. 30 (2020) 187–195.
[49] J. Xu, W. Zhang, H. Fan, et al., Nano Energy 51 (2018) 73–82.
[50] G. Zhou, H. Tian, Y. Jin, et al., Proc. Natl. Acad. Sci. U. S. A. 114 (2017) 840–845.
[51] K. Lv, P. Wang, C. Wang, et al., Small 16 (2020) 2000870.